Applied Catalysis B: Environmental 304 (2022) 121012

Contents lists available at ScienceDirect

Applied Catalysis B: Environmental

journal homepage: www.elsevier.com/locate/apcatb

Stress-induced $BiVO_4$ photoanode for enhanced photoelectrochemical performance

Weiyi Jiang [a], Yang An [b], Zeyan Wang [a,*], Minrui Wang [a], Xiaolei Bao [a], Liren Zheng [a], Hefeng Cheng [a], Peng Wang [a], Yuanyuan Liu [a], Zhaoke Zheng [a], Ying Dai [c], Baibiao Huang [a,*]

[a] State Key Lab of Crystal Materials, Shandong University, Jinan 250100, China
[b] Institute for Innovative Materials and Energy (School of Chemistry and Chemical Engineering), Yangzhou University, 225002 Yangzhou, Jiangsu, China
[c] School of Physics, Shandong University, Jinan 250100, China

ARTICLE INFO

Keywords:
Photoelectrochemical
$BiVO_4$ photoanode
Stress engineering
Water oxidation

ABSTRACT

$BiVO_4$ is a promising and environmental-benign photoanode material. However, the photoelectrochemical properties of $BiVO_4$ are confined to its low charge separation efficiency. Herein, we have developed a simple method to introduce stress into the $BiVO_4$ photoanode via the change of the unit cell volume of VO_2 near the phase transition temperature. In this way, the crystal structure of $BiVO_4$ is caused to be distorted and thus improve the photoelectrochemical properties of the $BiVO_4$ photoanode, making the surface photopotential of the $BiVO_4$-V photoanode nearly double that of the bare $BiVO_4$ photoanode. At room temperature, the photocurrent density of the $BiVO_4$-V photoanode is 2.35 times that of the $BiVO_4$ photoanode. Intriguingly, at 85 °C, the photocurrent density of the $BiVO_4$-V photoanode is as high as 6.8 times that of the $BiVO_4$ photoanode. Moreover, the photocurrent density of the $BiVO_4$-V photoanode could reach 80% of the theoretical photocurrent density of the $BiVO_4$ photoanode at 85 °C in the presence of the sacrificial agent Na_2SO_3. This work illustrates a new stress engineering strategy to improve the photoelectrochemical properties of $BiVO_4$ photoanodes and is expected to be applicable to other semiconductor photoanodes.

1. Introduction

In the quest for strategies to address environmental contamination and energy crisis, photoelectrochemical (PEC) water splitting technology has triggered a lot of interest owing to its low cost and high theoretical conversion efficiency [1–4]. Upon solar light illumination, semiconductor photoelectrodes yield photogenerated electrons and holes to produce hydrogen and oxygen from water splitting, respectively. Because of its good visible light absorption, suitable bandgap, and high photoelectric activity as well as great stability, bismuth vanadate ($BiVO_4$) has been regarded as one of the best-known candidates for highly efficient and stable metal oxide semiconductor photoanodes [5–9]. In theory, $BiVO_4$ photoanodes have a maximum photocurrent density of 7.5 mA/cm^2 and a solar to hydrogen (STH) conversion efficiency of 9.1% under AM 1.5 G irradiation [10]. For most conventional semiconductor photoelectrodes, the STH conversion efficiency is limited by the short carrier diffusion length, poor electrical conductivity, and slow oxidation kinetics, etc. In order to further improve the STH efficiency of $BiVO_4$ photoanodes, various technologies have been well developed involving ions doping, cocatalysts introduction, bandgap engineering, surface overlayer formation (hole transfer layer, HTL), and heterojunction construction (electron transfer layer, ETL). Unfortunately, the photovoltage of $BiVO_4$ photoanode is still limited by its band energy, and ultimately its conversion efficiency is constrained by the Shockley-Queisser (S-Q) limit [11–13].

Different from the photovoltaic effect of the traditional semiconductor materials, in some ferroelectric materials or piezoelectric materials with non-centrosymmetric crystal structures, the photovoltage can far exceed the bandwidth of the material itself, reaching several hundreds or even thousands of volts. This phenomenon is called the bulk photovoltaic (BPV) effect or anomalous photovoltaic (APV) effect [14–21]. Nonequilibrium hot electrons can be generated and effectively utilized in ferroelectric photovoltaic cells based on the BPV effect [22]. However, the BPV effect only exists in ferroelectric or piezoelectric semiconductor materials with non-centrosymmetric crystal structures, which greatly prevents the application of the BPV effect in photovoltaic

* Corresponding authors.
E-mail addresses: wangzeyan@sdu.edu.cn (Z. Wang), bbhuang@sdu.edu.cn (B. Huang).

https://doi.org/10.1016/j.apcatb.2021.121012
Received 25 September 2021; Received in revised form 24 November 2021; Accepted 10 December 2021
Available online 13 December 2021

devices. Recently, the BPV effect has also been reported in the semiconductor material with a centrally symmetric crystal structure. For example, Alexe et al. found that the stress was applied to $BaTiO_3$ to destroy its local symmetrical structure to achieve the BPV effect [23]. The BPV effect induced by stress is called the flexo-photovoltaic (FPV) effect. Therefore, the FPV effect is more universal and controllable than the BPV effect. Therefore, it is an effective technology to greatly improve the solar energy conversion efficiency of the photovoltaic device and even break the S-Q limit of the photovoltaic device to reach higher theoretical solar energy conversion efficiency.

Recently, a significant FPV effect has been found in $BiVO_4$ ceramics by stress applied to the $BiVO_4$ ceramics [24]. Under light illumination, a large open circuit voltage of 40 V could be obtained. This might provide a possibility to further improve the PEC conversion efficiency of $BiVO_4$ photoanodes based on the FPV effect. Mai et al. introduced BPV into $BiNbO_4$ thin film, increasing its photovoltage and photocurrent by 2 times and 10 times [25]. Fan et al. introduced the internal electric field by spontaneous polarization in the ferroelectric phase through the change of temperature to enhance the photocatalytic performance of $Sr_{0.7}Ba_{0.3}Nb_2O_6$ [26]. Huang et al. facilitated the charge separation of $BiOIO_3$ through enhancing its macroscopic polarization [27]. In addition, according to Ullah et al., changing the structure of semiconductors' bandgap can improve the photoelectrochemical properties of photoelectrodes [28–33]. Under these guidelines, we designed a simple method to introduce stress into $BiVO_4$ photoanode through room-temperature phase transition material VO_2, leading to the $BiVO_4$-V photoanode. VO_2 is a room temperature phase transition material that transforms from the monoclinic phase to the tetragonal phase at 68 °C. Through temperature variation to cause the phase transformation and volume expansion of VO_2, large stress can be introduced into the $BiVO_4$-V photoanode. By comparing the PEC properties of $BiVO_4$-V photoanode at different temperatures, the effect of stress on PEC water splitting of $BiVO_4$ photoanode can be demonstrated, illustrating a new approach to efficient semiconductor photoanodes for PEC water splitting.

2. Experimental details

2.1. Preparation of $BiVO_4$ photoanode

$BiVO_4$ photoanodes were prepared by a modified metal-organic decomposition method. Fluorine-doped SnO_2 coated glass (FTO) was cleaned ultrasonically in ethanol (99.0%; Aldrich) for 10 min, rinsed with distilled water, and dried. To prepare the $BiVO_4$ precursor solutions, $Bi(NO_3)_3{\cdot}5H_2O$ in glacial acetic acid (0.4 M, 1.8 mL), and vanadyl acetylacetonate (0.06 M, 12 mL) in acetylacetone were mixed with a Bi: V stoichiometric ratio of 1:1. The precursor solution was obtained after 20 min of ultrasonication at room temperature. The precursor solution was spin-coated on FTO substrates at 700 rpm for 10 s. And then the FTO substrates were dried at 150 °C for 10 min and calcined at 470 °C for 30 min. The above procedure was repeated for four cycles to obtain $BiVO_4$ photoanodes [34].

2.2. Preparation of $BiVO_4$-V photoanode

$BiVO_4$-V photoanodes were formed by a modified metal-organic decomposition method. FTO was cleaned ultrasonically in ethanol (99.0%; Aldrich) for 10 min, rinsed with distilled water, and dried. To prepare the $BiVO_4$-V precursor solution, $Bi(NO_3)_3{\cdot}5H_2O$ in glacial acetic acid (0.4 M, 1.8 mL) and vanadyl acetylacetonate (0.06 M, 12 mL) in acetylacetone were mixed with a Bi: V elemental stoichiometric ratio of 1:1. Then, 0.144 mmol vanadium dioxide (VO_2) was mixed with $BiVO_4$-V precursor solutions. After 20 min of ultrasonication at room temperature, the precursor solution was spin-coated on FTO substrates at 700 rpm for 10 s. Subsequently, the FTO substrates were dried at 150 °C for 10 min and calcined at 470 °C for 30 min. The above procedure was repeated for four cycles to obtain the $BiVO_4$-V photoanode.

2.3. Physical characterizations

The crystal structures of prepared photoanodes were characterized by X-ray diffraction (XRD) (Bruker D8 Advance X-ray diffractometer with Cu Kα irradiation, λ = 1.54 Å). The morphologies of prepared photoanodes were characterized by a Hitachi S-4800 scanning electron microscopy (SEM). The Raman spectra were characterized by an all solid state laser with a 632 nm laser source (Horiba Jobin Yvon HR800). The absorbance spectra were characterized by a Shimadzu UV 2550 UV–vis spectrometer. The thermogravimetric measurements were performed by a thermogravimetric analyzer (Diamond TG) in the air atmosphere. The HD-KFM measurements of as-prepared photoanodes were performed by an atomic force microscope (CSI Nano-Observer AFM). The surface compositions and bonding states of prepared photoanodes were evaluated by an X-ray photoelectron spectroscopy (Thermo Fisher Scientific Escalab-250, Al K). The surface photovoltaic spectroscopy (SPS) of prepared photoanodes is characterized by a surface photovoltage system (Ceaulight CEL-SP1000). Transmission electron microscopy (TEM) was measured by a JEOL-2011 transmission electron microscope with an accelerating voltage of 200 kV.

2.4. Photoelectrochemical measurements

Photoelectrochemical measurements of the as-prepared photoanodes were characterized in a 0.1 M potassium phosphate (pH = 7) by a three-electrode electrochemical cell configuration with a Pt sheet as the counter electrode, the prepared photoanode as the working electrode, and a saturated calomel electrode (SCE) as the reference electrode using a Princeton Applied Research EG&G 263A potentiostat. The results in the work are presented against the reversible hydrogen electrode (RHE) by using this equation:

$$E_{RHE} = E_{SCE} + 0.059 * pH + 0.241$$

All measurements were characterized under simulated sunlight provided by a 300 W Xe arc lamp (Perfectlight, Beijing, Co.LTD) coupled with an AM 1.5 G filter (100 mW/cm^2).

Applied bias photo to current conversion efficiency is calculated using photocurrent density and open circuit potential (V_{oc}) data by the following equation:

$$ABPE\ (\%) = \{(J_{\mathrm{pH}}\ (\mathrm{mA/cm^2}) * [1.23 - V_{app}\ (\mathrm{V})])/P\ (\mathrm{mA/cm^2})\} * 100$$

where J_{pH} = (light current − dark current)/area of the electrode, $V_{app} = V_{meas} - V_{oc}$ (V_{meas} is the potential which J_{pH} was recorded), and P is illumination intensity of the light source.

Electrochemical Impendence Spectra (EIS) analysis is carried out at 0 V *vs.* SCE under AM 1.5G illumination at a frequency range of 100 kHz to 0.1 Hz with an amplitude of 10 mV.

Charge separation efficiency at the electrode/electrolyte interface (η_{interf}) and in the bulk (η_{bulk}) of as-prepared photoanodes were calculated by the following equations:

$$\eta_{interf} = J_{pH}^{H_2O} / J_{pH}^{Na_2SO_3}$$

$$\eta_{bulk} = J_{pH}^{Na_2SO_3} / J_{abs}$$

$J_{pH}^{Na_2SO_3}$ and $J_{pH}^{H_2O}$ are the photocurrent densities measured in the electrolyte with and without Na_2SO_3 as the hole sacrificial agent. J_{abs} is the photon absorption rate expressed as the photocurrent density, and its calculation formula is as follow:

$$J_{abs} = \frac{q}{hc}\int_{\lambda} \lambda * \phi_{\lambda} * \eta_{abs} d\lambda$$

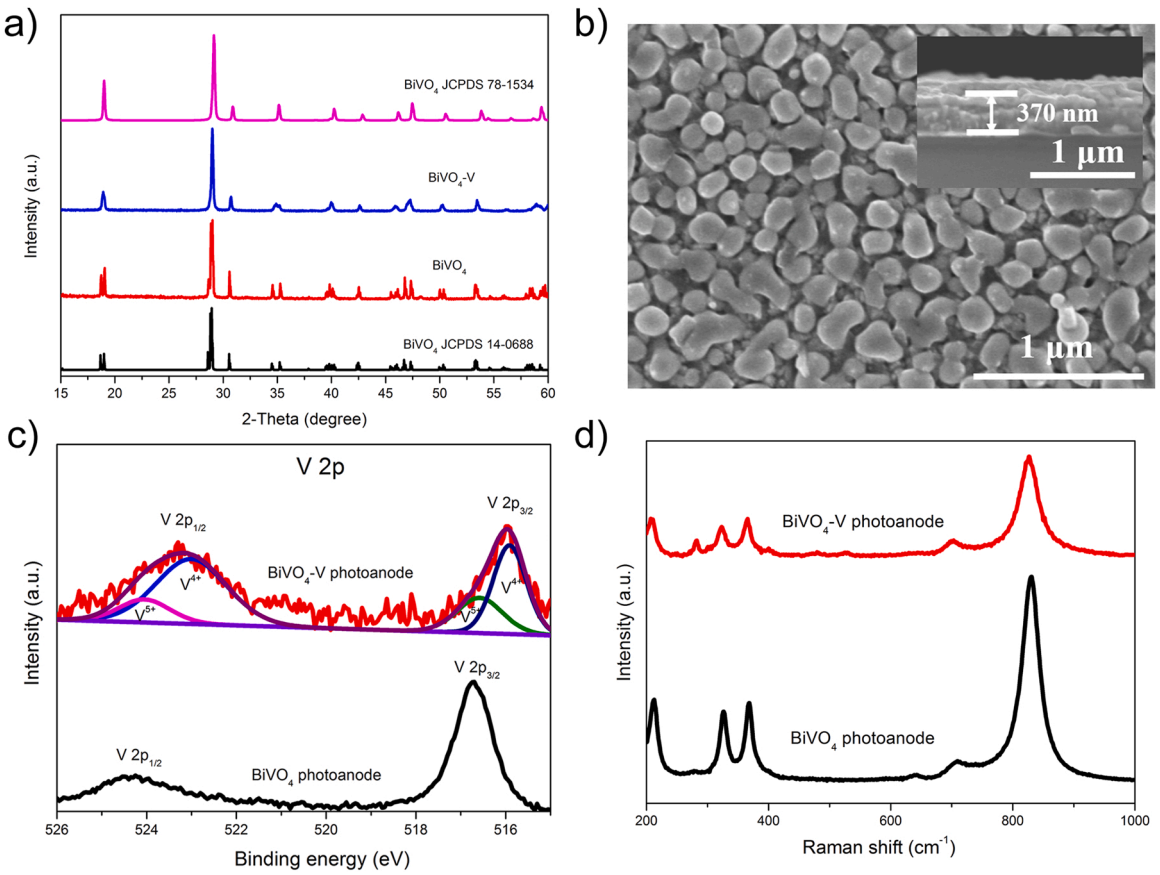

Fig. 1. (a) The XRD patterns of $BiVO_4$ and $BiVO_4$-V photoanodes. The XRD patterns of pure $BiVO_4$, a monoclinic $BiVO_4$ standard card (JCPDS 14-0688), and a high-pressure phase $BiVO_4$ (1.6 GPa) standard card (JCPDS 78-1534) are also listed. (b) The top view SEM image of $BiVO_4$-V photoanode. The inset of Fig. 1(b) shows the cross-sectional view SEM image of the as-synthesized $BiVO_4$-V photoanode. (c) V 2p XPS spectra of $BiVO_4$ and $BiVO_4$-V photoanodes. (d) Raman spectra of $BiVO_4$ and $BiVO_4$-V photoanodes at 25 °C, excited by a laser (632 nm).

Where h is the Plank constant, q is the charge of an electron, c is the speed of light, ϕ_λ is the photon flux of the AM 1.5G solar spectrum, η_{abs} is the absorbance of the photoanode.

3. Results and discussions

As shown in Fig. S1, the photoanode with Bi and V stoichiometric ratios of 1:1.2 has the highest photocurrent density at 25 and 85 °C. Therefore, the $BiVO_4$-V photoanode in this paper has Bi and V stoichiometric ratios of 1:1.2.

3.1. Characterizations and PEC performance of $BiVO_4$ and $BiVO_4$-V photoanodes at room temperature

As shown in the XRD patterns (Fig. 1**a**), the $BiVO_4$-V powder scraped from $BiVO_4$-V photoanodes has similar XRD diffraction peaks as $BiVO_4$ powder scraped from $BiVO_4$ photoanodes, corresponding to the monoclinic $BiVO_4$ (JCPDS 14-0688) [35]. Due to the low content and high dispersion of VO_2, the XRD diffraction peak of VO_2 could not be observed. However, from the locally enlarged XRD patterns, it is indicated that $BiVO_4$-V has significant changes compared with $BiVO_4$. For $BiVO_4$-V, the double XRD peaks (18–20°) corresponding to the $BiVO_4$ (1 1 0) and (0 1 1) crystal faces evolve into a single peak (Fig. S2a). The diffraction peaks corresponding to the $BiVO_4$ (1 2 1) and (0 4 0) crystal faces move toward a high angle (Fig. S2b and c). Furthermore, the diffraction peaks corresponding to the $BiVO_4$ (2 0 0) and (0 0 2) crystal faces gradually approach (Fig. S2d). The trend is similar to the XRD pattern of the high-pressure phase $BiVO_4$ (1.6 GPa) (JCPDS 78-1534). It is indicated that the as-synthesized $BiVO_4$-V has certain stress (< 1.6 GPa) and the symmetry of the $BiVO_4$ cell in as-synthesized $BiVO_4$-V photoanode is the tetragonal system. This stress may be due to the fact that $BiVO_4$ and VO_2 have different crystal structures and thermal expansion coefficients, resulting in a lattice mismatch at the $BiVO_4$-V interface.

The distortion of the crystal lattice had no obvious change on the nanoscopic morphology of the $BiVO_4$-V photoanode. As shown in the SEM images (Figs. 1**b** and S3), $BiVO_4$ photoanode and $BiVO_4$-V photoanode are both comprised of many irregular nanoparticles. The average diameters of the nanoparticles in $BiVO_4$ and $BiVO_4$-V photoanodes are 150 nm and 225 nm, respectively. The cross-sectional view SEM images (insets of Figs. 1**b** and S3) indicate that the average thicknesses of $BiVO_4$ and $BiVO_4$-V photoanodes are 420 nm and 370 nm, respectively. Fig. S4 shows the HR-TEM image of $BiVO_4$-V photoanode, the plane spacing between (1 0 2) lattice corresponding to VO_2, and the plane spacing between (0 4 0) lattice corresponding to $BiVO_4$ are 0.268 and 0.292 nm, respectively. The lattice fringes of VO_2 are sturdily joined with those of $BiVO_4$, which indicates the VO_2 has been doped into $BiVO_4$ photoanode.

The light absorption of VO_2 powder, as-synthesized $BiVO_4$ and $BiVO_4$-V photoanodes were measured by a UV–vis spectrophotometer equipped with an integrating sphere. As shown by the DRS in Fig. S5, both the absorption edges of the $BiVO_4$ and $BiVO_4$-V photoanodes are located at about 500 nm. It indicates that the addition of VO_2 has no significant effect on the light absorption of the $BiVO_4$ photoanode.

The existence of VO_2 in the $BiVO_4$-V photoanode and the change of metal-oxygen bond length could be confirmed by X-ray photoemission spectroscopy (XPS). The XPS spectra indicates the chemical environment information of vanadium, bismuth, and oxygen in the two as-synthesized samples (Figs. 1**c** and S6). In $BiVO_4$ photoanode, the V 2p

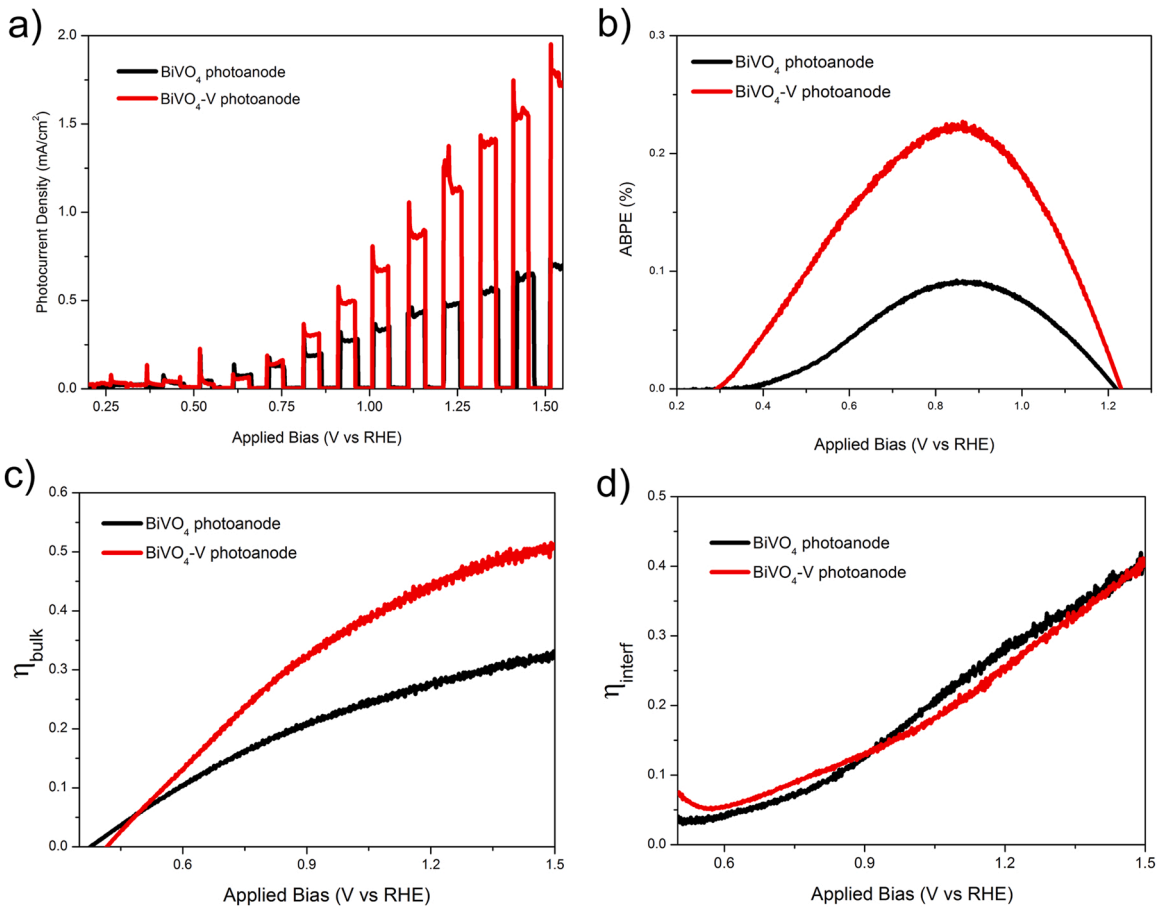

Fig. 2. (a) Photocurrent density *vs.* applied potential curves (J-V) of $BiVO_4$ and $BiVO_4$-V photoanode with a scan rate of 10 mV/s under irradiation of AM 1.5 G simulated solar light (100 mW/cm^2) in 0.1 M potassium phosphate electrolyte solution at 25 °C. (b) ABPE curves of as-synthesized $BiVO_4$ and $BiVO_4$-V photoanode at 25 °C. Charge separation efficiency (c) in the bulk (η_{bulk}) and (d) at the electrode/electrolyte interface (η_{interf}) of $BiVO_4$ and $BiVO_4$-V photoanode at 25 °C.

peak centers are located at 516.7 and 524.35 eV, respectively [36]. In contrast, the V 2p peak of the $BiVO_4$-V photoanode shifted to the lower binding energy of 515.97 and 523.27 eV [37], respectively. The peak of V $2p_{3/2}$ can be deconvoluted into two components representing the V^{4+} (VO_2 515.9 eV) and the V^{5+} ($BiVO_4$ 516.7 eV), and the peak of V $2p_{1/2}$ can also be deconvoluted into two components representing the V^{4+} (VO_2 523 eV) and the V^{5+} ($BiVO_4$ 523.9 eV). It indicated that some low valence vanadium (in the form of VO_2) exists in the as-synthesized $BiVO_4$-V photoanode. However, Bi 4f peak centers of $BiVO_4$ and $BiVO_4$-V did not shift significantly (Fig. S6a) [38]. It indicated the chemical environment of bismuth has not changed caused by VO_2 introduced. The O 1s peak of as-synthesized $BiVO_4$ and $BiVO_4$-V photoanodes can be fitted to two peaks: lattice oxygen (O_L, 529.79 eV, and 529.72 eV) and chemisorbed or dissociated oxygen species (O_C, 531.8 eV) [39]. As shown in Fig. S6b, compared to $BiVO_4$, the lattice oxygen peak center of $BiVO_4$-V shifted from 529.79 eV to 529.72 eV. This smaller banding energy indicates that the metal-oxygen bond length are increased and the crystal structure of $BiVO_4$ are changed.

The structural information was further characterized by Raman spectra. Fig. 1**d** displays Raman spectra of the as-synthesized $BiVO_4$ photoanode and $BiVO_4$-V photoanode at room temperature excited by a laser (632 nm). The Raman bands around 210, 324, 366, 640, 700, and 830 cm^{-1} were observed for all samples, which are the typical vibrational bands of $BiVO_4$. Specifically, the 210 cm^{-1} Raman band is an external mode of $BiVO_4$ with almost no structural information. The 324 and 366 cm^{-1} Raman bands are the asymmetric and symmetric deformation modes of the VO_4^{3-} tetrahedron in $BiVO_4$. The 700 and 830 cm^{-1} Raman bands are the stretching modes of two different types of V–O bonds. In contrast, the Raman band around 281 cm^{-1} was observed for the $BiVO_4$-V photoanode. This Raman band is the typical vibrational band of VO_2, suggesting the presence of VO_2 in the sample. The stretching modes of the shorter V-O bond around 830 cm^{-1} of $BiVO_4$-V photoanode shifted to lower frequencies compared with those of $BiVO_4$ photoanode. According to Brown et al. [40–43], the empirical expression relating the V-O bond length to the Raman stretching frequencies is as follow:

$$\nu[\mathrm{cm}^{-1}] = 21349 * \exp(-1.9176R\ [\text{Å}]) \quad (1)$$

Therefore, the V—O bond lengths in $BiVO_4$ photoanode and $BiVO_4$-V photoanode, are calculated to be 1.693 Å and 1.696 Å, respectively. It indicates that doping VO_2 into the $BiVO_4$ photoanode changes the crystal structure of $BiVO_4$ in the $BiVO_4$-V photoanode.

The VO_2 added to the $BiVO_4$-V photoanode could also be obtained from the abnormal Bi: V ratio in the EDS spectrum. The EDS spectrum of $BiVO_4$-V photoanode (Fig. S7) is shown that the Bi: V elemental stoichiometric ratio is 1:1.17. It is basically consistent with the Bi: V ratio we used.

The $BiVO_4$ photoanode and $BiVO_4$-V photoanode yield the photocurrent density of 0.48 and 1.13 mA/cm^2 at 1.23 V *vs.* RHE, respectively (Fig. 2**a**). Calculated by the J-V curves, assuming 100% Faradaic efficiency, the applied bias photo-to-current efficiencies (ABPE) of the $BiVO_4$ photoanode and $BiVO_4$-V photoanode are shown in Fig. 2**b**. The maximum ABPE of the $BiVO_4$ photoanode and $BiVO_4$-V photoanode are 0.08% and 0.238%, respectively. These efficiencies are achieved at 0.92 V *vs.* RHE. The increased photocurrent and ABPE of $BiVO_4$-V photoanode can be explained by the improvement of charge separation

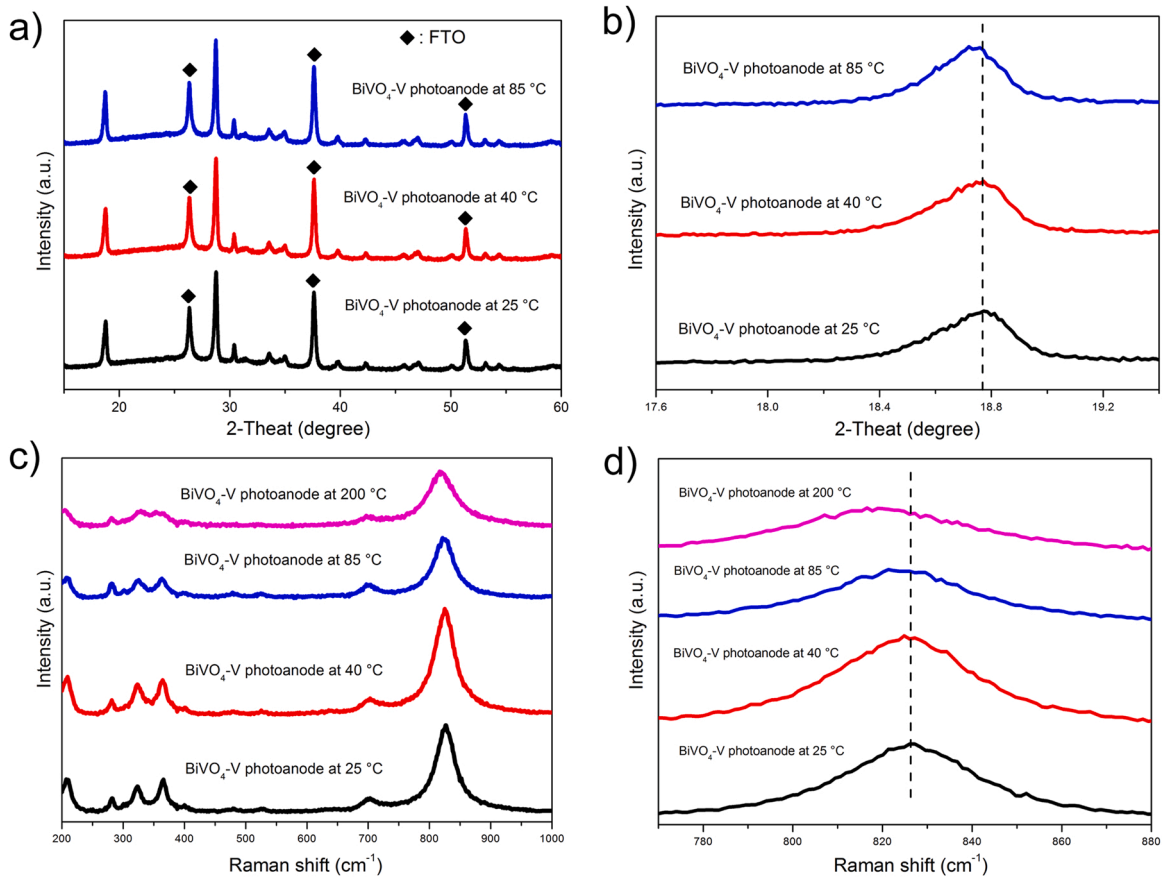

Fig. 3. (**a**) The XRD patterns of $BiVO_4$-V photoanode at 25, 40, and 85 °C. (**b**) Enlarged the XRD patterns of $BiVO_4$-V photoanode at 25, 40, and 85 °C. (**c**) Raman spectra of $BiVO_4$-V photoanode at 25, 40, and 85 °C, excited by a laser (632 nm). (**d**) Enlarged the Raman spectra of $BiVO_4$-V photoanode at 25, 40, and 85 °C.

efficiency in the bulk of $BiVO_4$-V photoanode (Fig. 2**c**). At the bias of 1.23 V *vs.* RHE, the calculated η_{bulk} of $BiVO_4$ photoanode and $BiVO_4$-V photoanode are 0.28 and 0.45, respectively. However, the charge separation efficiencies at the electrode/electrolyte interface of $BiVO_4$ photoanode and $BiVO_4$-V photoanode do not have a significant difference. At the bias of 1.23 V *vs.* RHE, the calculated η_{interf} of $BiVO_4$ photoanode and $BiVO_4$-V photoanode are 0.29 and 0.27, respectively (Fig. 2**d**). It is believed that stress can significantly enhance the charge separated efficiency in the bulk of $BiVO_4$-V photoanode compared with the $BiVO_4$ photoanode.

The surface photopotential mapping of the sample was also measured. As shown in Fig. S8, the surface photopotential of $BiVO_4$-V photoanode is nearly 2 times higher than that of the $BiVO_4$ photoanode at 25 °C. This further confirms that the surface photopotential of the $BiVO_4$-V photoanode was significantly improved compared with the $BiVO_4$ photoanode. It is believed that stress can significantly enhance the separated efficiency of photogenerated electrons and holes of $BiVO_4$-V photoanode compared with the $BiVO_4$ photoanode, and which is consistent with the measurement results of PEC.

3.2. Effect of temperature on the crystal structure and PEC performance of $BiVO_4$-V photoanode

As shown in the XRD patterns (Fig. 3**a**), the $BiVO_4$-V photoanodes at 25, 40, and 85 °C have similar XRD diffraction peaks. Due to the low content and high dispersion of VO_2, the XRD diffraction peak of VO_2 could not be observed. However, the locally enlarged XRD patterns (Fig. 3**b**) indicates that the crystal structure of $BiVO_4$-V photoanode at 85 °C has changed compared with the crystal structures of $BiVO_4$-V photoanodes at 25 and 40 °C. For $BiVO_4$-V photoanode at 85 °C, the XRD peak centers shift from 18.78° (the XRD peak centers of $BiVO_4$-V photoanodes at 25 and 40 °C) to 18.73°. According to the Bragg's Law, the lattice parameters of as-synthesized $BiVO_4$-V photoanodes at 25 and 85 °C correspond to a, $b = 5.1618$ Å, $c = 11.7417$ Å, $V = 312.848$ Å^3 and a, $b = 5.1687$ Å, $c = 11.7538$ Å, $V = 314.008$ Å^3, respectively (Table. S1). And the interplanar spacing of $BiVO_4$-V photoanode at 85 °C is greater than that of $BiVO_4$-V photoanodes at 25 and 40 °C. It indicated that the $BiVO_4$ unit cells of $BiVO_4$-V photoanode are under the tension stress caused by the VO_2 and with the increase of temperature, the tension stress became greater by the volume expansion of the VO_2 cell.

The structural information was further characterized by Raman spectra. Fig. 3**c** displays Raman spectra of as-synthesized $BiVO_4$-V photoanodes at 25 °C, 40 °C, and 85 °C excited by a laser (632 nm), respectively. Except for the Raman band around 830 cm^{-1}, all samples have a similar Raman band. The 830 cm^{-1} Raman band is the stretching mode of V—O bonds. This stretching mode of V—O bond around 830 cm^{-1} for $BiVO_4$-V photoanode at 85 °C shifted to lower frequencies compared with that of $BiVO_4$-V photoanodes at 25 and 40 °C. According to Formula (1), the V—O bond lengths in $BiVO_4$-V photoanode at 25 °C, $BiVO_4$-V photoanode at 40 °C, and $BiVO_4$-V photoanode at 85 °C are calculated to be 1.696 Å, 1.696 Å, and 1.698 Å, respectively. This indicates that the crystal structure of $BiVO_4$ in the $BiVO_4$-V photoanode changes when the temperature is higher than the VO_2 phase transition point. It is thus believed that the stress generated by the volume expansion caused by the phase transition of VO_2 is that the $BiVO_4$ unit cell is distorted.

In order to further verify that VO_2 causes changes in the structure of $BiVO_4$ around its phase transition temperature, it was characterized by thermal analysis. As shown in Fig. S9b, the $BiVO_4$-V powder scraped from the $BiVO_4$-V photoanode has a distinct endothermic peak at 70 °C,

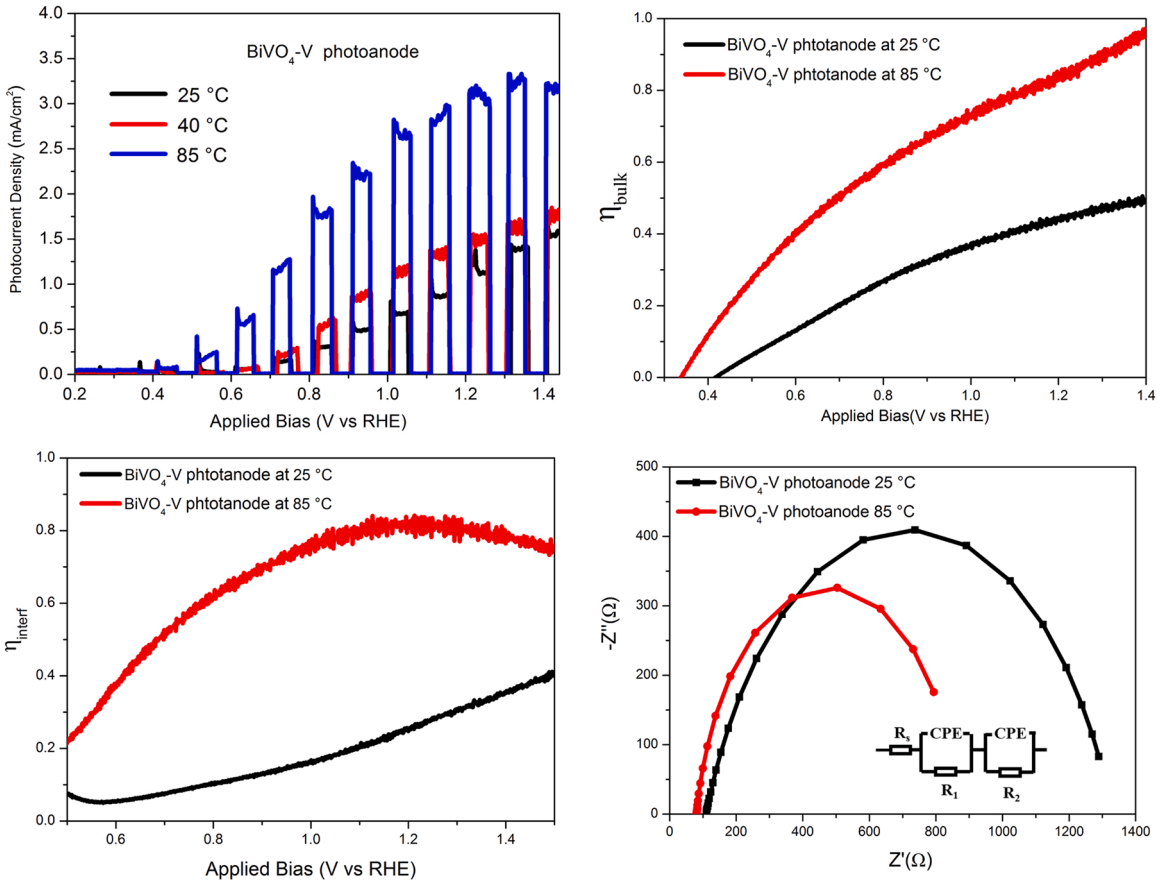

Fig. 4. (**a**) J-V curves of $BiVO_4$-V photoanode with a scan rate of 10 mV/s under irradiation of AM 1.5G simulated solar light (100 mW/cm^2) in 0.1 M potassium phosphate electrolyte solution at 25 °C, 40 °C, and 85 °C. Charge separation efficiency (**b**) in the bulk (η_{bulk}) and (**c**) at the electrode/electrolyte interface (η_{interf}) of $BiVO_4$-V photoanode at 25 °C and 85 °C. (**d**) Nyquist plots of $BiVO_4$-V photoanode measured at 25 °C and 85 °C (0 V *vs.* RHE) under light irradiation.

indicating the corresponding phase transformation. However, the $BiVO_4$ powder scraped from the $BiVO_4$ photoanode (Fig. S9a) has no obvious endothermic peak and exothermic peak, which proved that the $BiVO_4$ powder has no obvious phase transition at the test temperature range. It proves that $BiVO_4$ doped by VO_2 also has a phase transition around 70 °C.

The effect of stress on the PEC properties of $BiVO_4$ photoanodes was investigated at three different temperatures (25 °C, 40 °C, and 85 °C). The photocurrent density of the $BiVO_4$ photoanode does not change significantly at different temperatures, indicating that the temperature has no effect on the PEC properties of the $BiVO_4$ photoanode (Fig. S10). In contrast, the photocurrent density of $BiVO_4$-V photoanode is significantly improved with increasing temperature (Fig. 4**a**). At 40 °C, the photocurrent density of $BiVO_4$-V photoelectrode is measured to be 1.42 mA/cm^2, slightly higher than that at room temperature. Intriguingly, when the temperature is raised to 85 °C, the photocurrent density of $BiVO_4$-V photoanode can reach 3.31 mA/cm^2, which is 2.76 times of the photocurrent density measured at 25 °C. Compared with the $BiVO_4$ photoanode, the photocurrent densities of the $BiVO_4$-V photoanode at 25 °C, 40 °C, and 85 °C are 2.35, 2.95, and 6.80 times that of the $BiVO_4$ photoanode at the same conditions, respectively. The ABPE of $BiVO_4$-V photoanode at 25 and 85 °C based on the J-V curves are 0.238% and 0.765% at 0.92 V *vs.* RHE, respectively (Fig. S11). With Na_2SO_3 as a sacrificial agent at 85 °C, the theoretical photocurrent of the $BiVO_4$-V photoanode can reach 6 mA/cm^2 (Fig. S12). In this case, it could achieve 80% of the highest theoretical photocurrent of the $BiVO_4$ photoanode. If $BiVO_4$-V photoanode is optimized in such structure and conductivity, the photocurrent density is expected to further increase.

The increased photocurrent of the $BiVO_4$-V photoanode could be explained by the improvement of charge separation efficiency at the electrode/electrolyte interface and in the bulk of $BiVO_4$-V photoanode. Fig. 4**b, c** show the calculated η_{bulk} and η_{interf} of $BiVO_4$-V photoanode at 25 and 85 °C, respectively. At the bias of 1.23 V *vs.* RHE, the $\eta_{bulk,}$ and η_{interf} of the $BiVO_4$-V photoanode at 25 °C are 0.45 and 0.26, respectively. However, η_{bulk} and η_{interf} of $BiVO_4$-V photoanode increased to 0.86 and 0.83 at 85 °C, which was 1.91 and 3.19 times that at 25 °C. As described above, with the increase of temperature, the bulk and interfacial charge efficiency of $BiVO_4$-V photoanode is significantly improved.

In order to further verify the effect of temperature on the electron transport of $BiVO_4$-V photoanode, the electrochemical impedance spectroscopy (EIS) of $BiVO_4$-V photoanode was measured under illumination (AM 1.5G). The Nyquist plots of $BiVO_4$-V photoanode at 25 °C and 85 °C were shown in Fig. 4**d**, the charge transfer resistance of $BiVO_4$-V photoanode at 85 °C is 794 Ω, which is 65% of that at 25 °C. Compared with the charge transfer resistance of $BiVO_4$ photoanode (Fig. S13), the resistance of $BiVO_4$ photoanode is 1209.8 Ω and 1111.4 Ω at 25 and 85 °C, respectively. It indicates that the temperature has no effect on the charge transfer resistance of the $BiVO_4$ photoanode. Therefore, the reason for the decrease in the charge transfer resistance of the $BiVO_4$-V photoanode is believed to be associated with the distorted crystal structure of $BiVO_4$. The change of $BiVO_4$-V photoanode band structure could also improve its charge separation efficiency. As shown in Fig. S14, the valence band maximum (VBM) of $BiVO_4$ in $BiVO_4$-V photoanode is 3.08 eV *vs.* RHE, and VBM of $BiVO_4$ in $BiVO_4$ photoanode is 2.26 eV *vs.* RHE. According to the flat band diagram of $BiVO_4$ and $BiVO_4$-V photoanodes (Fig. S15), the stress in $BiVO_4$-V photoanode lifts the VBM upward by 0.82 eV compared to $BiVO_4$ photoanode. The VBM

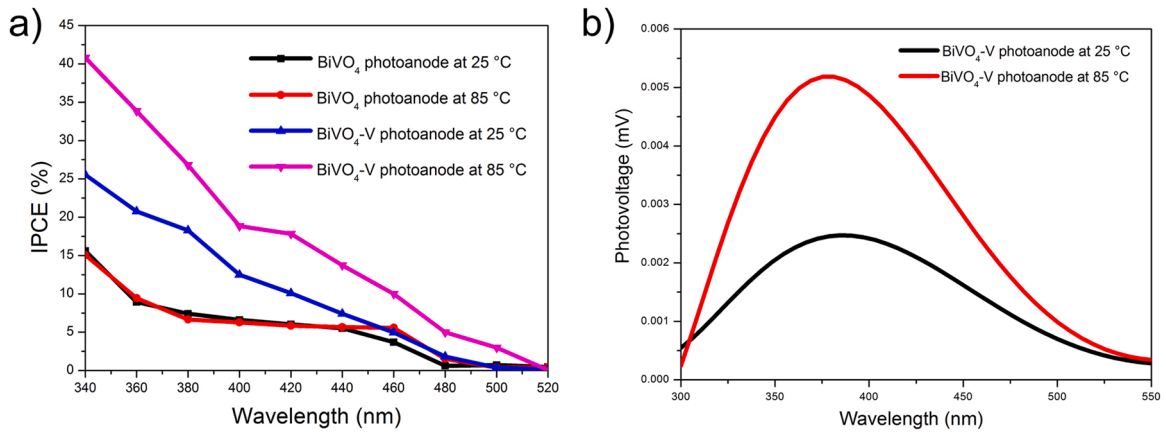

Fig. 5. (**a**) The incident photo-to-current conversion efficiencies (IPCEs) of $BiVO_4$ and $BiVO_4$-V photoanodes at 25 and 85 °C at a bias of 1.23 V *vs.* RHE. (**b**) The surface photovoltaic spectroscopy (SPS) of $BiVO_4$-V photoanode at 25 and 85 °C.

of $BiVO_4$ in $BiVO_4$-V photoanode is more conducive to the transportation of photon-generated holes to FTO, thereby improving the charge separation efficiency of $BiVO_4$-V photoanode.

The IPCEs of as-synthesized $BiVO_4$ and $BiVO_4$-V photoanodes at 25 and 85 °C were shown in Fig. 5**a**. The $BiVO_4$ photoanode at 25 and 85 °C has the same IPCEs (6.3% at the wavelength of 400 nm). However, the IPCEs value of $BiVO_4$-V photoanode at 25 and 85 °C are around 12.8% and 19.1% at the wavelength of 400 nm. It indicates that the temperature has no effect on the photoelectrochemical properties of $BiVO_4$ photoanode.

As shown in Fig. 5**b**, the surface photovoltage of $BiVO_4$-V photoanodes is responded at the range from 300 to 550 nm. However, the surface photovoltage of $BiVO_4$-V photoanode at 85 °C is around 0.005 mV, which is 2 times of the $BiVO_4$-V photoanode at 25 °C (0.0025 mV). It indicates that the separated efficiency of photogenerated electrons and holes of $BiVO_4$-V photoanode can be further improved at a higher temperature, which is consistent with the measured results of IPCE and PEC.

4. Conclusions

In summary, we have synthesized the $BiVO_4$-V photoanode to introduce stress into $BiVO_4$ through the VO_2 phase transition. At the temperature above the phase transition point, the unit cell volume of VO_2 is greatly increased and the stress in the $BiVO_4$-V photoanode is further increased, thus leading to the partial deformation in the crystal structure of $BiVO_4$. The dependence of the photocurrent of $BiVO_4$-V photoanode on temperature is the same as the trend of VO_2 cell volume variation. The results illustrate that by introducing stress into the $BiVO_4$ photoanode, the PEC water splitting properties can be effectively improved by adjusting the internal stress of the $BiVO_4$ photoanode. This stress engineering strategy could be applicable to other semiconductor materials to improve the PEC water splitting performance.

CRediT authorship contribution statement

B.H., **Z.W.**, and **H.C.** conceived and designed the project. **W.J.** performed the experiments and analyzed the data. **Y.A.** and **M.W.** offered help in the material characterizations. **X.B.**, **L.Z.**, **P.W.**, **Y.L.**, **Z. Z.**, and **Y.D.** offered help in the data analysis. **W.J.** and **H.C.** wrote the manuscript. All the authors discussed the results and commented on the manuscript.

Declaration of Competing Interest

The authors declare that they have no known competing financial interests or personal relationships that could have appeared to influence the work reported in this paper.

Acknowledgments

This work was financially supported by the National Natural Science Foundation of China (Nos. 22072072, 21802087, 51972195, 21832005, 21972078, and U1832145), National Key Research and Development Program of China (2020YFA0710301), Shandong University Multidisciplinary Research and Innovation Team of Young Scholars (2020QNQT11, 2020QNQT012), Natural Science Foundation of Shandong Province (ZR2019QB005), Qilu Young Scholars and Outstanding Young Scholars Projects of Shandong University, Taishan Scholar Foundation of Shandong Province.

Appendix A. Supporting information

Supplementary data associated with this article can be found in the online version at doi:10.1016/j.apcatb.2021.121012.

References

[1] H. Li, F. Li, Z. Wang, Y. Jiao, Y. Liu, P. Wang, X. Zhang, X. Qin, Y. Dai, B. Huang, Fabrication of carbon bridged g-C_3N_4 through supramolecular self-assembly for enhanced photocatalytic hydrogen evolution, Appl. Catal. B 229 (2018) 114–120, https://doi.org/10.1016/j.apcatb.2018.02.026.

[2] D. Xing, P. Zhou, Y. Liu, Z. Wang, P. Wang, Z. Zheng, Y. Dai, M. Whangbo, B. Huang, Atomically dispersed cobalt-based species anchored on polythiophene as an efficient electrocatalyst for oxygen evolution reaction, Appl. Surf. Sci. 545 (2021), 148943, https://doi.org/10.1016/j.apsusc.2021.148943.

[3] Y. An, Y. Liu, P. An, J. Dong, B. Xu, Y. Dai, X. Qin, X. Zhang, M. Whangbo, B. Huang, Ni-II coordination to Al-based metal-organic framework made from 2-aminoterephthalate for photocatalytic overall water splitting, Angew. Chem. Int. Ed. 56 (2017) 1–6, https://doi.org/10.1002/anie.201612423.

[4] F. Niu, D. Wang, F. Li, Y. Liu, S. Shen, T.J. Meyer, Hybrid photoelectrochemical water splitting systems: from interface design to system assembly, Adv. Energy Mater. 10 (11) (2019), 1900399, https://doi.org/10.1002/aenm.201900399.

[5] Y. Qiu, W. Liu, W. Chen, W. Chen, G. Zhou, P. Hsu, R. Zhang, Z. Liang, S. Fan, Y. Zhang, Y. Cui, Efficient solar-driven water splitting by nanocone $BiVO_4$ perovskite tandem cells, Sci. Adv. 2 (6) (2016), e1501764, https://doi.org/10.1126/sciadv.1501764.

[6] M. Lamers, S. Fiechter, D. Friedrich, F.F. Abdi, R. van de Krol, Formation and suppression of defects during heat treatment of $BiVO_4$ photoanodes for solar water splitting, J. Mater. Chem. A 6 (38) (2018) 18694–18700, https://doi.org/10.1039/C8TA06269B.

[7] Y. Pihosh, I. Turkevych, K. Mawatari, J. Uemura, Y. Kazoe, S. Kosar, K. Makita, T. Sugaya, T. Matsui, D. Fujita, M. Tosa, M. Kondo, T. Kitamori, Photocatalytic generation of hydrogen by core-shell WO_3/$BiVO_4$ nanorods with ultimate water splitting efficiency, Sci. Rep. 5 (1) (2015) 11141, https://doi.org/10.1038/srep11141.

[8] G. Zhang, Y. Meng, B. Xie, Z. Ni, H. Lu, S. Xia, Precise location and regulation of active sites for highly efficient photocatalytic synthesis of ammonia by facet-dependent $BiVO_4$ single crystals, Appl. Catal. B 296 (2021), 120379, https://doi.org/10.1016/j.apcatb.2021.120379.

[9] S. Ju, H. Kang, J. Jun, S. Son, J. Park, W. Kim, H. Lee, Periodic micropillar-patterned FTO/$BiVO_4$ with superior light absorption and separation efficiency for efficient PEC performance, Small 17 (20) (2021), 2006558, https://doi.org/10.1002/smll.202006558.

[10] H.W. Jeong, T.H. Jeon, J.S. Jang, W. Choi, H. Park, Strategic modification of $BiVO_4$ for improving photoelectrochemical water oxidation performance, J. Phys. Chem. C 117 (18) (2013) 9104–9112, https://doi.org/10.1021/jp400415m.

[11] S.J. Strickler, J.R. Bolton, J.S. Connolly, Limiting and realizable efficiencies of solar photolysis of water, Nature 316 (6028) (1985) 495–500, https://doi.org/10.1038/316495a0.

[12] W. Shockley, H.J. Queisser, Detailed balance limit of efficiency of p-n junction solar cells, J. Appl. Phys. 32 (3) (1961) 510–519, https://doi.org/10.1063/1.1736034.

[13] J.Y. Kim, J. Lee, H.S. Jung, H. Shin, N. Park, High-efficiency perovskite solar cells, Chem. Rev. 120 (15) (2020) 7867–7918, https://doi.org/10.1021/acs.chemrev.0c00107.

[14] T. Choi, S. Lee, Y.J. Choi, V. Kiryukhin, S.W. Cheong, Switchable ferroelectric diode and photovoltaic effect in $BiFeO_3$, Science 5923 (324) (2009) 63–66, https://doi.org/10.1126/science.1168636.

[15] Z. Chen, T.F. Jaramillo, T.G. Deutsch, A. Kleiman-Shwarsctein, A.J. Forman, N. Gaillard, R. Garland, K. Takanabe, C. Heske, M. Sunkara, E.W. McFarland, K. Domen, E.L. Miller, J.A. Turner, H.N. Dinh, Accelerating materials development for photoelectrochemical hydrogen production: standards for methods, definitions, and reporting protocols, J. Mater. Res. 25 (1) (2010) 3–16, https://doi.org/10.1557/JMR.2010.0020.

[16] C. Paillard, X. Bai, I.C. Infante, M. Guennou, G. Geneste, M. Alexe, J. Kreisel, B. Dkhil, Photovoltaics with ferroelectrics: current status and beyond, Adv. Mater. 28 (26) (2016) 5153–5168, https://doi.org/10.1002/adma.201505215.

[17] S.Y. Yang, J. Seidel, S.J. Byrnes, P. Shafer, C.H. Yang, M.D. Rossell, P. Yu, Y.H. Chu, J.F. Scott, J.W. Ager, L.W. Martin, R. Ramesh, Above-bandgap voltages from ferroelectric photovoltaic devices, Nat. Nanotechnol. 5 (2) (2010) 143–147, https://doi.org/10.1038/nnano.2009.451.

[18] R. Nechache, C. Harnagea, S. Li, L. Cardenas, W. Huang, J. Chakrabartty, F. Rosei, Bandgap tuning of multiferroic oxide solar cells, Nat. Photonics 9 (1) (2015) 61–67, https://doi.org/10.1038/nphoton.2014.255.

[19] B. Kim, J. Kim, N. Park, First-principles identification of the charge-shifting mechanism and ferroelectricity in hybrid halide perovskites, Sci. Rep. 10 (1) (2020) 19635, https://doi.org/10.1038/s41598-020-76742-7.

[20] Y.J. Zhang, T. Ideue, M. Onga, F. Qin, R. Suzuki, A. Zak, R. Tenne, J.H. Smet, Y. Iwasa, Enhanced intrinsic photovoltaic effect in tungsten disulfide nanotubes, Nature 570 (7761) (2019) 349–353, https://doi.org/10.1038/s41586-019-1303-3.

[21] D. Pang, X. Liu, X. He, C. Chen, J. Zheng, Z. Yi, Anomalous photovoltaic effect in Bi$(Ni_{2/3}Ta_{1/3})O_3$-$PbTiO_3$ ferroelectric solid solutions, J. Am. Ceram. Soc. 102 (6) (2019) 3448–3456, https://doi.org/10.1111/jace.16184.

[22] J.E. Spanier, V.M. Fridkin, A.M. Rappe, A.R. Akbashev, A. Polemi, Y. Qi, Z. Gu, S. M. Young, C.J. Hawley, D. Imbrenda, G. Xiao, A.L. Bennett-Jackson, C.L. Johnson, Power conversion efficiency exceeding the Shockley-Queisser limit in a ferroelectric insulator, Nat. Photonics 10 (9) (2016) 611–616, https://doi.org/10.1038/nphoton.2016.143.

[23] M. Yang, D.J. Kim, M. Alexe, Flexo-photovoltaic effect, Science 6391 (360) (2018) 904–907, https://doi.org/10.1126/science.aan3256.

[24] X. Liu, F. Zhang, P. Long, T. Lu, H. Zeng, Y. Liu, R.L. Withers, Y. Li, Z. Yi, Anomalous photovoltaic effect in centrosymmetric ferroelastic $BiVO_4$, Adv. Mater. 30 (44) (2018), 1801619, https://doi.org/10.1002/adma.201801619.

[25] H. Mai, T. Lu, Q. Sun, J. Langley, N. Cox, F. Kremer, T. Duong, K. Catchpole, H. Chen, Z. Yi, T.J. Frankcombe, Y. Liu, Defect engineering for creating and enhancing bulk photovoltaic effect in centrosymmetric materials, J. Mater. Chem. A 9 (22) (2021) 13182–13191, https://doi.org/10.1039/D1TA02699B.

[26] Dayong Fan, Ruifeng Chong, Fengtao Fan, Xiuli Wang, Can Li, Zhaochi Feng, A tetragonal tungsten bronze-type photocatalyst: ferro-paraelectric phase transition and photocatalysis, Chin. J. Catal. 37 (8) (2016) 1257–1262, https://doi.org/10.1016/S1872-2067(15)61126-3.

[27] H. Huang, S. Tu, C. Zeng, T. Zhang, A.H. Reshak, Y. Zhang, Macroscopic polarization enhancement promoting photo-and piezoelectric-induced charge separation and molecular oxygen activation, Angew. Chem. Int. Ed. 56 (39) (2017) 11860–11864, https://doi.org/10.1002/anie.201706549.

[28] M.F.R. Samsudin, H. Ullah, A.A. Tahir, X. Li, Y.H. Ng, S. Sufian, Superior photoelectrocatalytic performance of ternary structural $BiVO_4$/GQD/g-C_3N_4 heterojunction, J. Colloid Interface Sci. 586 (2021) 785–796, https://doi.org/10.1016/j.jcis.2020.11.003.

[29] H. Ullah, A.A. Tahir, S. Bibi, T.K. Mallick, S.Z. Karazhanov, Electronic properties of β-TaON and its surfaces for solar water splitting, Appl. Catal. B 229 (2018) 24–31, https://doi.org/10.1016/j.apcatb.2018.02.001.

[30] H. Ullah, A.A. Tahir, T.K. Mallick, Structural and electronic properties of oxygen defective and Se-doped p-type $BiVO_4$ (0 0 1) thin film for the applications of photocatalysis, Appl. Catal. B 224 (2018) 895–903, https://doi.org/10.1016/j.apcatb.2017.11.034.

[31] J. Safaei, H. Ullah, N.A. Mohamed, M.F. Mohamad Noh, M.F. Soh, A.A. Tahir, N. Ahmad Ludin, M.A. Ibrahim, W.N.R. Wan Isahak, M.A. Mat Teridi, Enhanced photoelectrochemical performance of Z-scheme g-C_3N_4/$BiVO_4$ photocatalyst, Appl. Catal. B 234 (2018) 296–310, https://doi.org/10.1016/j.apcatb.2018.04.056.

[32] S.N.F.M. Nasir, H. Ullah, M. Ebadi, A.A. Tahir, J.S. Sagu, M.A. Mat Teridi, New insights into Se/$BiVO_4$ heterostructure for photoelectrochemical water splitting: a combined experimental and DFT study, J. Phys. Chem. C 121 (11) (2017) 6218–6228, https://doi.org/10.1021/acs.jpcc.7b01149.

[33] M.F.R. Samsudin, H. Ullah, R. Bashiri, N.M. Mohamed, S. Sufian, Y.H. Ng, Experimental and DFT insights on microflower g-C_3N_4/$BiVO_4$ photocatalyst for enhanced photoelectrochemical hydrogen generation from lake water, ACS Sustain. Chem. Eng. 8 (25) (2020) 9393–9403, https://doi.org/10.1021/acssuschemeng.0c02063.

[34] H. Zhang, H. Li, Z. Wang, Z. Zheng, P. Wang, Y. Liu, X. Zhang, X. Qin, Y. Dai, B. Huang, Fabrication of $BiVO_4$ photoanode consisted of mesoporous nanoparticles with improved bulk charge separation efficiency, Appl. Catal. B 238 (2018) 586–591, https://doi.org/10.1016/j.apcatb.2018.07.050.

[35] Y. Ji, J. Cao, L. Jiang, Y. Zhang, Z. Yi, G-C_3N_4/$BiVO_4$ composites with enhanced and stable visible light photocatalytic activity, J. Alloy. Compd. 590 (2014) 9–14, https://doi.org/10.1016/j.jallcom.2013.12.050.

[36] M. Li, G. Xu, Z. Guan, Y. Wang, H. Yu, Y. Yu, Synthesis of Ag/$BiVO_4$/rGO composite with enhanced photocatalytic degradation of triclosan, Sci. Total Environ. 664 (2019) 230–239, https://doi.org/10.1016/j.scitotenv.2019.02.027.

[37] R. Cui, S. Yu, P. Han, Y. Wu, Y. Li, Y. Dang, Y. Zhou, J. Zhu, Novel vacancy-rich Co_3O_4/VO_2 nanohybrids for enhanced electrocatalytic performance and application as oxygen evolution electrocatalysts, J. Alloy. Compd. 876 (2021), 160129, https://doi.org/10.1016/j.jallcom.2021.160129.

[38] L. Jinhai, M. Han, Y. Guo, F. Wang, L. Meng, D. Mao, S. Ding, C. Sun, Hydrothermal synthesis of novel flower-like $BiVO_4$/$Bi_2Ti_2O_7$ with superior photocatalytic activity toward tetracycline removal, Appl. Catal. A 524 (2016) 105–114, https://doi.org/10.1016/j.apcata.2016.06.025.

[39] Y.M. Hunge, A. Uchida, Y. Tominaga, Y. Fujii, A.A. Yadav, S. Kang, N. Suzuki, I. Shitanda, T. Kondo, M. Itagaki, M. Yuasa, S. Gosavi, A. Fujishima, C. Terashima, Visible light-assisted photocatalysis using spherical-shaped $BiVO_4$ photocatalyst, Catalysts 11 (4) (2021) 460, https://doi.org/10.3390/catal11040460.

[40] A. Galembeck, O.L. Alves, $BiVO_4$ thin film preparation by metalorganic decomposition, Thin Solid Films 365 (2000) 90–93, https://doi.org/10.1016/S0040-6090(99)01079-2.

[41] J. Yu, A. Kudo, Effects of structural variation on the photocatalytic performance of hydrothermally synthesized $BiVO_4$, Adv. Funct. Mater. 16 (2006) 2163–2169, https://doi.org/10.1002/adfm.200500799.

[42] S.M. Thalluri, C. Martinez Suarez, M. Hussain, S. Hernandez, A. Virga, G. Saracco, N. Russo, Evaluation of the parameters affecting the visible-light-induced photocatalytic activity of monoclinic $BiVO_4$ for water oxidation, Ind. Eng. Chem. Res. 52 (2013) 17414–17418, https://doi.org/10.1021/ie402930x.

[43] Y.K. Kho, W.Y. Teoh, A. Iwase, L. Mädler, A. Kudo, R. Amal, Flame preparation of visible-light-responsive $BiVO_4$ oxygen evolution photocatalysts with subsequent activation via aqueous route, ACS Appl. Mater. Interfaces 3 (2011) 1997–2004, https://doi.org/10.1021/am200247y.